applied sciences

MDPI

Article

Comparative Study of Droplet Diameter Distribution: Insights from Experimental Imaging and Computational Fluid Dynamics Simulations

Kasimhussen Vhora [1,2,*], Gábor Janiga [2], Heike Lorenz [1], Andreas Seidel-Morgenstern [1], Maria F. Gutierrez [1] and Peter Schulze [1]

[1] Physical and Chemical Foundations of Process Engineering, Max Planck Institute for Dynamics of Complex Technical Systems, 39106 Magdeburg, Germany; lorenz@mpi-magdeburg.mpg.de (H.L.); seidel@mpi-magdeburg.mpg.de (A.S.-M.); gutirrezsnchez@mpi-magdeburg.mpg.de (M.F.G.); schulzep@mpi-magdeburg.mpg.de (P.S.)

[2] Laboratory of Fluid Dynamics and Technical Flows, University of Magdeburg "Otto von Guericke", Universitätsplatz 2, 39106 Magdeburg, Germany; janiga@ovgu.de

* Correspondence: vhora@mpi-magdeburg.mpg.de

Abstract: The interfacial area between two phases plays a crucial role in the mass transfer rate of gas–liquid processes such as absorption. In this context, the droplet size distribution within the flow field of a droplet-based absorber significantly affects the surface area, thereby influencing the absorption efficiency. This study focuses on developing a computational fluid dynamics (CFD) model to predict the size and distribution of water droplets free-falling in a transparent square tube. This model serves as a digital twin of our experimental setup, enabling a comparative analysis of experimental and computational results. For the accurate measurement of droplet size and distribution, specialized experimental equipment was developed, and a high-speed camera along with Fiji software was used for the capturing and processing of droplet images. At the point of injection and at two different heights, the sizes and distributions of falling droplets were measured using this setup. The interaction between the liquid water droplets and the gas phase within the square tube was modeled using the Eulerian–Lagrangian (E-L) framework in the STAR-CCM+ software. The E-L multiphase CFD model yielded approximations with errors ranging from 11 to 27% for various average mean diameters, including d_{10}, d_{20}, d_{30}, and d_{32}, of the liquid droplets at two distinct heights (200 mm and 400 mm) for both nozzle plates. This comprehensive approach provides valuable insights into the dynamics of droplet-based absorption processes.

Keywords: droplet size; experimental validation; computational fluid dynamics; multiphase flow; Eulerian–Lagrangian modeling

Citation: Vhora, K.; Janiga, G.; Lorenz, H.; Seidel-Morgenstern, A.; Gutierrez, M.; Schulze, P. Comparative Study of Droplet Diameter Distribution: Insights from Experimental Imaging and Computational Fluid Dynamics Simulations. *Appl. Sci.* **2024**, *14*, 1824. https://doi.org/10.3390/app14051824

Academic Editor: Satoru Okamoto

Received: 31 December 2023
Revised: 19 February 2024
Accepted: 20 February 2024
Published: 23 February 2024

1. Introduction

Droplet size measurement is critical in a wide range of industries and scientific research disciplines. With the help of this thorough knowledge, a variety of processes from spray drying to fuel injection in car engines can be optimized to work as efficiently and effectively as possible [1]. There are several methods used to measure droplet size and distribution. Common methods include optical microscopy, laser scattering, and light scattering [2–4]. These methodologies necessitate the use of specialized equipment, specifically, a high-speed camera equipped with an appropriate zoom lens. This equipment is employed to accurately measure droplet size and distribution, particularly in scenarios characterized by high-velocity flows. On the other hand, CFD (computational fluid dynamics) simulation is a powerful tool for understanding fluid dynamics and the transport of mass and heat in gas–liquid systems. CFD simulation can provide detailed information about the flow field in single-phase and multiphase flow systems [5].

Different studies have focused on the CFD simulation of spray-based equipment using different approaches. The use of CFD for the assessment of evaporative cooling by water spray systems, particularly in urban settings, was highlighted by Montazeri et al. (2015), who also demonstrated the precision of the Lagrangian–Eulerian approach when tested against wind-tunnel results [6]. Nijdam et al. (2006) compared the Eulerian and Lagrangian modeling approaches for turbulent dispersion and droplet coalescence within a spray, and they came to the conclusion that the Lagrangian approach was more feasible in terms of implementation and applicability [7]. An axisymmetric population balance model for spray drying was created by Pinto et al. (2014), who emphasized the importance of capturing the precise droplet size distribution and how it relates to drying kinetics [8]. Chot-Plassot et al. (2022) argued for a well-balanced combination of both CFD and experimental methodologies to improve spray releases [9], whereas Beji et al. (2017) investigated the influence of parameters such as droplet size distribution on CFD simulations and computing time [10]. Together, these works highlight the expanding body of evidence supporting the usefulness of CFD in understanding and predicting droplet behavior, as well as the necessity of incorporating experimental data for strong validations.

Applications ranging from combustion systems to environmental controls depend heavily on monitoring the distribution of droplet sizes. To simulate urea-water sprays in selective catalytic reduction systems, Frühhaber et al. (2020) used CFD, demonstrating the skill of air-assisted nozzles in obtaining the best ammonia homogenization [11]. A novel technique was developed by Mahmud et al. (2022) to measure the median diameter of water-mist spray droplets, a crucial factor that affects fire extinguishing procedures [12]. To mimic the aerodynamic breakage of droplets, Rossano and De Stefano (2022) introduced a hybrid Volume of Fluid (VOF)–Lagrangian technique, providing a thorough response to the problems associated with liquid fragmentation [13]. The importance of accurate droplet measurements and the possibility of CFD validations in improving industrial applications are both emphasized by these works. Understanding droplet size and distribution in various flow regimes is crucial for optimizing industrial processes. Dimiccoli et al. (2000) underscored the role of droplet distribution in determining the efficiency of absorption processes, emphasizing the relationship between droplet characteristics and mass transfer in spray-tower loop absorbers [14]. Saber et al. (2022) furthered this understanding through a numerical study, revealing how parameters such as injection velocity and nozzle radius affect droplet distribution in turbulent jet flow [15]. Meanwhile, Bade et al. (2010) combined experimental and computational approaches to investigate droplet dynamics at varying injection angles, showcasing the importance of angles in droplet formation and behavior [16]. Tamhankar's work in 2015 provided an in-depth analysis of spray absorption, offering rigorous measurements of droplet sizes across multiple spray-plume locations while also correlating the influence of solvents, such as MEA, on droplet characteristics [17,18]. Furthermore, Cho et al. (2018) introduced a novel spray-tower design to efficiently capture carbon dioxide (CO_2) emissions using a uniform spray of mono-sized absorbent droplets. The research explored a potential solution for capturing CO_2, contributing to the advancement of carbon capture technologies [19]. Foissac et al. (2011) focused on droplet distributions in reactor containment nozzles [20].

Cents et al. (2004) explored the use of ultrasound for determining droplet and particle size distributions, focusing on the propagation speed of ultrasound. Their research, which showcased the precision of ultrasound in discerning droplet sizes, emphasized the potential of further validation using digital camera techniques [21]. Meanwhile, in the context of shear-driven atomization, Kastengren et al. (2017) employed ultra-small-angle X-ray scattering (USAXS), presenting significant findings, including the observed absence of nanoscale droplets, a factor that challenged prevailing models [22]. Frommhold et al. (2014) incorporated ultrasound in a novel manner, producing monodisperse droplets through ultrasonically controlled micro-jet breakup, thus adding to the scope of methodologies available for precise droplet measurement [23].

The droplet sizes and velocities in air-atomized sprays were examined by Musiu et al. (2019) using CFD, with a focus on the impact of nozzle flow rates and sprayer distance on droplet distribution, which they validated using the Malvern Mastersizer 2000 [24]. Cao et al. (2022) studied the interaction between droplets and moving leaves, which is essential for efficient agricultural spraying [25]. Lastly, Wirz et al. (2022) explored droplet size distributions in stirred vessels, leveraging a convolutional neural network for precise measurements and uncovering how operational parameters influence droplet size [26]. Collectively, these studies emphasize the significance of employing advanced techniques for measuring droplet diameters and distributions and conducting simulations to gain a deeper comprehension of droplet dynamics.

In general, the combination of high-speed cameras and CFD simulations provides a powerful tool for understanding and optimizing gas–liquid systems. With the availability of high-speed cameras with higher frame rates and higher resolutions, the measurement of droplet size and distribution will become even more accurate and effective.

Many existing studies in the field of CFD that focus on modeling droplet size and distribution primarily pertain to scenarios involving spray nozzles or jet flows. In these studies, the Volume of Fluid (VOF) CFD model has often been employed, despite its computational expense in comparison to the more efficient Eulerian model [27]. This method is not suitable for simulating a droplet absorber with multiple nozzles due to its high computational cost.

The measurement of droplet size and distribution using a high-speed camera and validation through CFD simulations are effective techniques for understanding and optimizing gas–liquid systems. In the present study, the assessment and characterization of water droplet size distribution utilized the less resource-intensive Eulerian–Lagrangian [27] approach. This method divides the gas-droplet flow into two distinct models: the continuous phase, described by the Eulerian model, and the discrete phase, represented by the Lagrangian model. Our primary objective in this research was to ascertain the size distribution of droplets produced by two nozzle plates. To achieve this, we employed a high-speed camera equipped with a zoom lens to capture images of droplet formation at the time of inception and at two different heights: 200 mm and 400 mm. Subsequently, we analyzed these droplet images using the open-source Fiji software (version 1.53t) [28] to determine their respective sizes. The resulting droplet size distribution data were then graphed, and an attempt was made to fit them to established distribution models such as the log-normal, Gaussian, or normal distributions. At the injection point, the distribution model that best aligned with our empirical data was subsequently used as the input for our CFD multiphase flow simulation to predict droplet diameter distribution along the square tube.

The CFD simulations were performed to validate their results against experimental measurements of droplet distribution. The literature mainly combines experimental methods with CFD to study single-nozzle sprays. The present study, however, used a nozzle plate with multiple nozzles. CFD simulations were used to predict the droplet diameter distribution from this nozzle plate, and these predictions were then validated with experimental results. The primary aim of this research was to identify an appropriate CFD model capable of accurately predicting droplet size and distribution, with the intention of validating its performance against experimental data. Once validated, this CFD model holds potential for applicability in predicting the fluid dynamics and droplet size distribution of alternative geometric configurations within the system.

2. Experimental and Computational Numerical Methods

2.1. Experimental Setup

To perform this study, a special experimental setup was built, as shown in Figure 1.

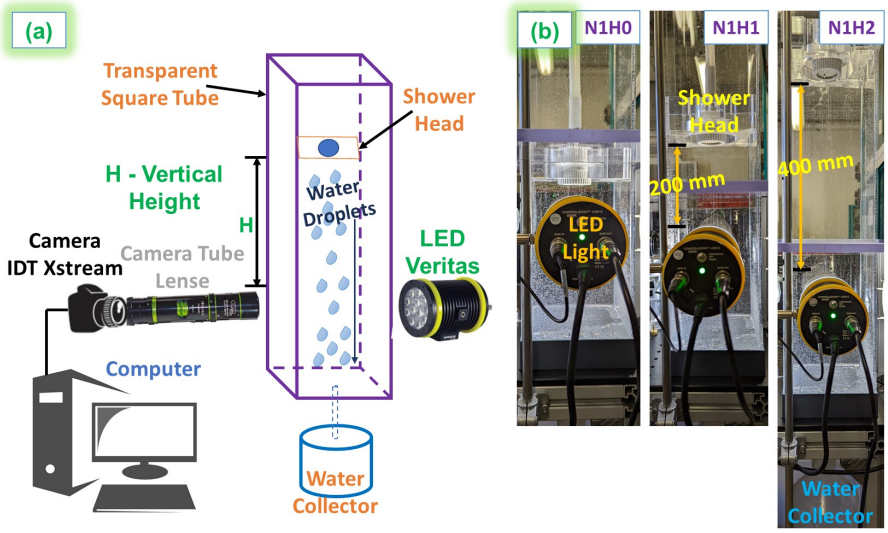

Figure 1. (**a**) Schematic diagram of acquisition of droplets. (**b**) Experimental setup for acquisition of droplets.

The 1000 mm high transparent square tube (150 × 150 mm) was made from Poly methyl methacrylate (PMMA—acrylic glass) material, with a movable nozzle plate head placed in it. On one side of the square tube, an LED light source (Veritas–Constellation 120E15 with a power of 48VDC in) was placed, and on the opposite side, a high-speed camera (IDT XStream PCIe series with Camera Tube Lens MINI 2X 400 FL 35-08-14-000 Optem Fusion) was positioned, as displayed in Figure 1a. Two different kinds of nozzle plates made from various materials and with varying numbers of nozzles were used in this study. Figure 1b illustrates the experimental setup across three distinct scenarios, denoted as H0, H1, and H2. In scenario H0, the camera frame was positioned with no vertical separation from the shower head. In scenario H1, a vertical gap of 200 mm between the camera frame and the shower head was introduced, whereas in scenario H2, this distance was increased to 400 mm. N1 refers to a type of nozzle featuring 17 individual nozzles.

2.1.1. Acquisition of Falling Droplets

The shower head with the nozzle plate was placed in the transparent square tube at 0, 200, and 400 mm, respectively, above the high-speed camera's focus frame so that droplets could be captured at different heights from the nozzle plate head. Distilled water was pumped into the nozzle plate head, generating different sizes of droplets based on the size of the nozzle and flow rate. Droplets were ejected vertically downward. The flow rate for each nozzle plate was selected to ensure that the formation of the droplets occurred in the Rayleigh jet breakup regime. In this regime, the predominant breakup mechanism is the surface tension force [29]. The definition of a certain breakup regime is a combination of different variables, such as the liquid velocity inside the nozzle and the density, viscosity, and surface tension of the fluid. In order to ensure the breakup regime, the Reynolds number of the liquid (Re) should fulfill the condition given in Equation (1), where Oh is the Ohnesorge number. This equation was obtained from the relation between Re and Oh in the first transition of the breakup regime (from the Rayleigh jet breakup to the first wind-induced breakup) [29]. The Reynolds number can be related to the volumetric flow rate, as presented in Equation (2), and the Ohnesorge number can be related to the fluid properties, as presented in Equation (3). In these equations, n is the number of nozzles, d_0 is the nozzle diameter, ρ_l is the liquid density, μ_l is the liquid viscosity, $\dot{q}_l$ is the flow rate, and σ_l is the liquid surface tension. Generally, the Rayleigh regime occurs with a Weber

number less than 0.4, as reported in the literature [29], and the average droplet diameter is approximately twice the nozzle outlet diameter ($d = 1.89d_0$) [30].

$$\mathrm{Re} \leq 45.973(\mathrm{Oh})^{-1.3069} \quad (1)$$

$$\mathrm{Re} = \frac{4\dot{q}_l\rho_l}{n\pi d_0\mu_l} \quad (2)$$

$$\mathrm{Oh} = \frac{\mu_l}{(\rho_l\sigma_l d_0)^{0.5}} \quad (3)$$

Afterward, images of droplets falling from the nozzle plate head in the transparent square tube were captured by the high-speed camera for the various experimental cases (N1H0 to N2H2). In this context, N1 represents the nozzle type, including parameters such as the nozzle number and material. The variable H signifies the various distances from the nozzle plate at which the droplet images were taken. For instance, H0 denotes a vertical distance of 5 mm between the nozzle and the high-speed camera, whereas H1 corresponds to a distance of 200 mm, and so on. A comprehensive description of the experimental runs is presented in Table 1. Subsequently, the sizes of the falling droplets were measured using image analysis software, specifically Fiji, after capturing the images with a high-speed camera.

Table 1. Details of experimental runs.

Exp. Run	Number of Nozzles	Nozzle Diameter, µm	Nozzle Plate Material	Flow Rate, L/hr	Vertical Height (H), mm
N1H0	17	170 ± 5	PEEK	3.6	0
N1H1	17	170 ± 5	PEEK	3.6	200
N1H2	17	170 ± 5	PEEK	3.6	400
N2H0	30	200 ± 5	SS1.4310	7	0
N2H1	30	200 ± 5	SS1.4310	7	200
N2H2	30	200 ± 5	SS1.4310	7	400

In this study, we utilized two different types of nozzle plates, and the diameter of the nozzle outlet for each plate was measured using a Keyence Digital Microscope VHX-2000. We determined the average nozzle size (N1: 170 µm; N2: 200 µm) to calculate the inlet water flow rate for each nozzle plate based on the number of nozzles in each respective plate. More information regarding the nozzle sizes, their corresponding flow rates, and the materials used in their construction is shown in Table 1. N1 featured 17 nozzles, whereas N2 incorporated a total of 30 nozzles within the nozzle plate. Both nozzle plates had a thickness of 0.5 mm.

2.1.2. Image Acquisition and Post-Processing

In total, 6 different experimental cases were studied and analyzed (N1H0 to N2H2), as shown in Table 1. In each case, a total of 1000 captured frames were used to measure the sizes of the droplets and their distribution. Fiji (Fiji Is Just ImageJ) is an open-source image-processing package based on ImageJ2 [31], bundling a lot of plugins that facilitate scientific image analysis [28]. Fiji was utilized to post-process 1000 frames for each case to measure the sizes of the droplets.

The method for enumerating the sizes of the droplets using Fiji required the image file to be converted from RGB to 8-bit grayscale, as illustrated in Figure 2a,b. The automated counting of droplets used threshold algorithms to discriminate the features of interest from the background. The threshold level was dependent on the algorithm selected, and in this image analysis, the Yen threshold algorithm was used [32].

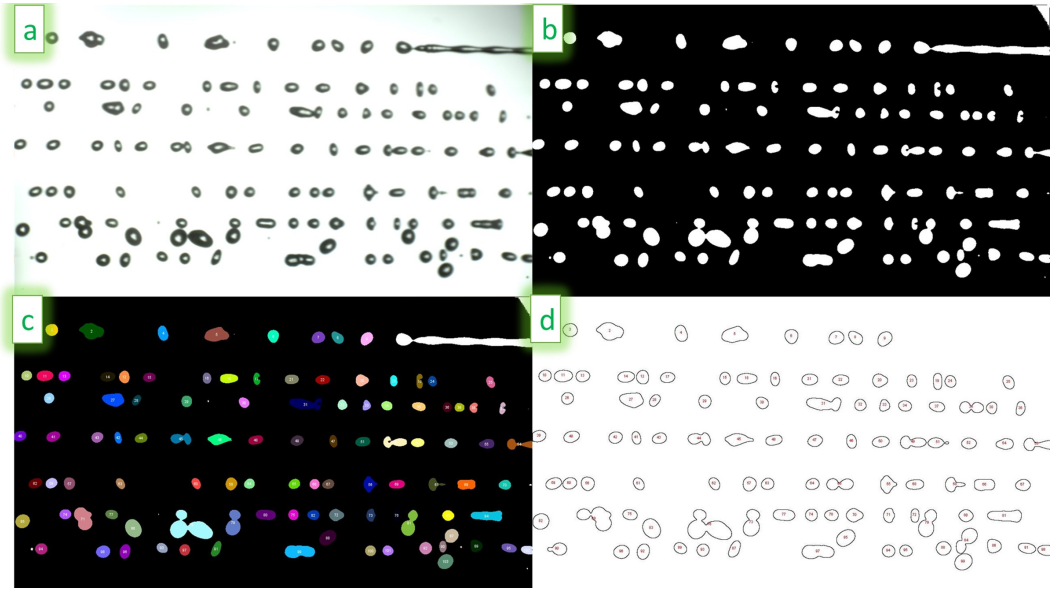

Figure 2. Case N1H0: (**a**) Raw image of the acquisition of droplets. (**b**) Conversion of image from RGB to 8-bit grayscale. (**c**) Identification of droplets to calculate pixel sizes. (**d**) Calculation of droplets' diameters.

To establish the counting threshold, the procedure began by opening the selected image. The following sequence of steps was then meticulously executed: navigating through 'Image > Adjust > Threshold', selecting the appropriate algorithm, and applying it to convert the image into a binary format, as illustrated in Figure 2b. This conversion was achieved by choosing 'Process > Binary > Make binary'. Subsequently, droplet counting was conducted using 'Analyze > Analyze Particles'. During this process, the droplet size parameters were set with an area range of 50/200–infinity pixels and a circularity range of 0.8–1. Each droplet counted was outlined and numbered in a separate window, as shown in Figure 2d. Subsequently, the pixel area of each of these outlined droplets was calculated, and from this area, the diameter was determined in pixel units. Finally, to obtain the actual droplet size of each identified droplet, the pixel area was converted using a pixel size value of 10.75 µm/pixel (calculated from camera calibration). Details regarding camera calibration and nozzle size measurements can be found in the Supplementary Material Figures S1–S3. Notably, this same image analysis technique has been employed in biological cell size measurement, as documented in the literature [33]. From each droplet diameter size, we further calculated various average mean diameters (d_{10}, d_{20}, d_{30}, and d_{32}) of the liquid droplets. The arithmetic mean diameter, denoted as d_{10}, represents the average diameter of all particles within a given sample.

$$d_{10} = \frac{\sum n_i d_i}{N} \tag{4}$$

In contrast, the surface mean diameter d_{20}, refers to the diameter of a particle whose surface area, when multiplied by the total number of droplets, equals the overall surface area of the sample.

$$d_{20} = \left[\frac{\sum n_i d_i^2}{N}\right]^{1/2} \tag{5}$$

The volume mean diameter, d_{30}, signifies the diameter of a particle whose volume, when multiplied by the total particle count, matches the total volume of the sample.

$$d_{30} = \left[\frac{\sum n_i d_i^3}{N}\right]^{1/3} \tag{6}$$

Lastly, the term "d_{32} diameter" refers to the Sauter mean diameter (SMD), which characterizes the average size of particles in a sample. It is specifically defined as the diameter of a sphere that has the same volume-to-surface area ratio as the droplet of interest [34].

$$d_{32} = \frac{\sum n_i d_i^3}{\sum n_i d_i^2} \tag{7}$$

In these definitions, n_i represents the count of droplets falling in the focused camera frame i, whereas d_i denotes the corresponding representative water droplet diameter in the same frame. The summations encompass all particles, with N representing the total count of droplets.

2.2. CFD Digital Twin of Experimental Setup

In computational fluid dynamics, a computerized replication of an experimental setup is established to enable in-depth studies and examinations. The CFD digital twin, as depicted in Figure 3a, was utilized for the investigation of droplet size and distribution for 4 different cases (N1H1, N1H2, N2H1, and N2H2) and later validated with experimental results. For each simulation case, the corresponding log-normal distribution for the droplet size was used as input. For the N1H1 and N1H2 cases, the distribution from 17 droplet injection points in Figure 4 was used, whereas for the N2H1 and N2H2 cases, the distribution from 30 droplet injection points in Figure 5 was utilized.

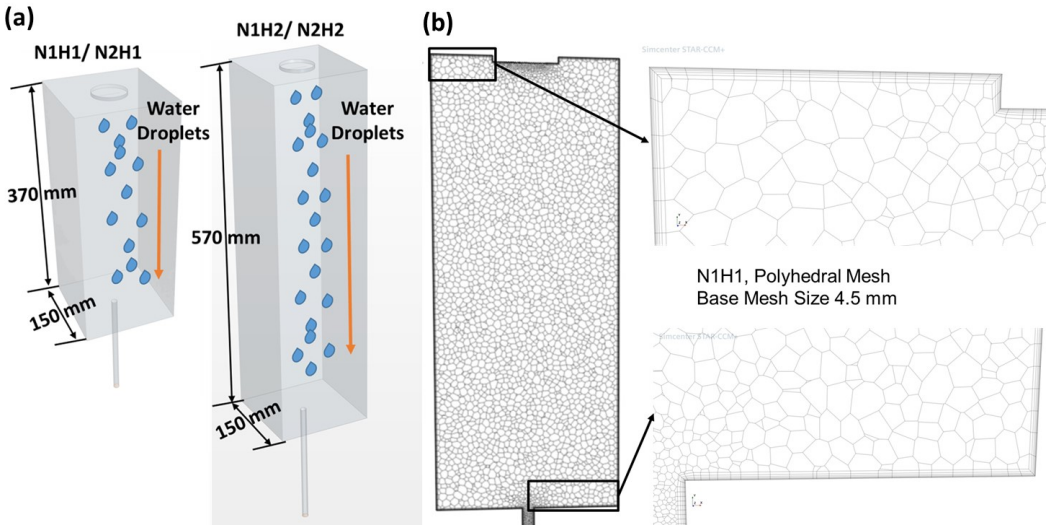

Figure 3. (**a**) Digital twin of the experimental setup. (**b**) Polyhedral meshing of CFD setup for N1H1.

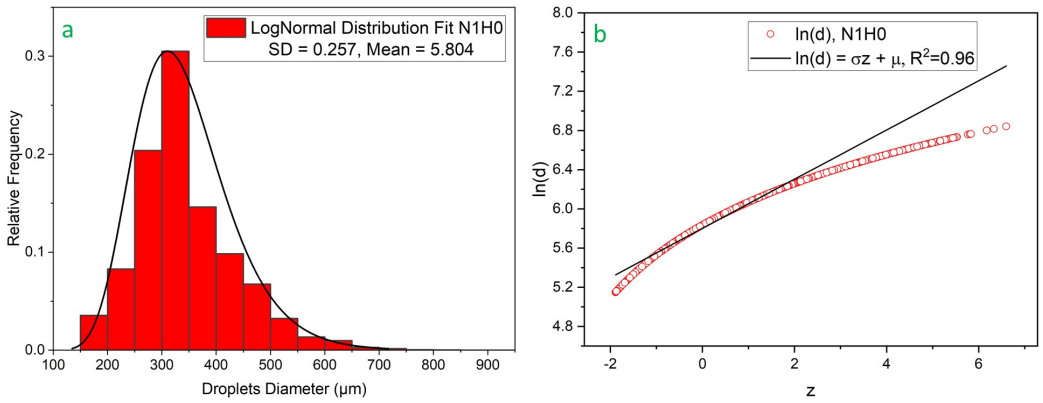

Figure 4. (**a**) Experimental droplet size frequency distribution with fitted curve. (**b**) Log−normal distribution fitting with linear fit of R^2 for N1H0.

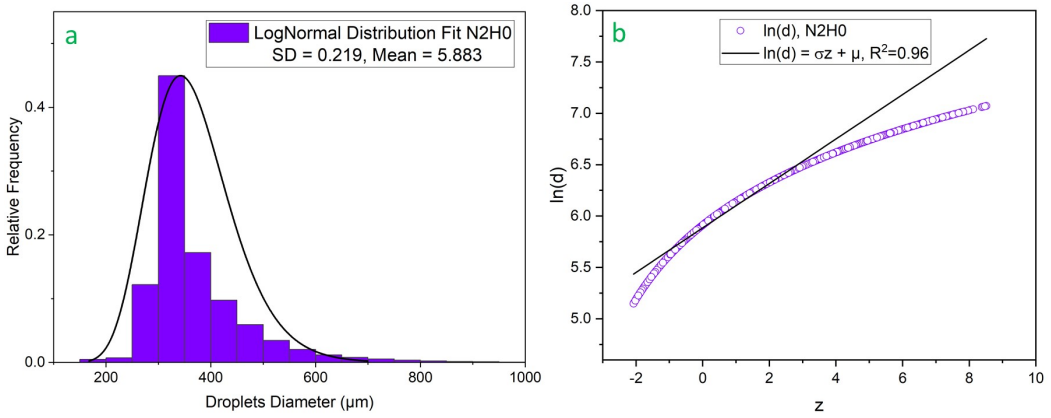

Figure 5. (**a**) Experimental droplet size frequency distribution with fitted curve. (**b**) Log−normal distribution fitting with linear fit of R^2 for N2H0.

To conduct the CFD simulations, a volumetric domain was constructed based on the provided digital twin geometry (Figure 3a). This domain was subsequently partitioned into discrete cells to establish a mesh. In all the CFD simulations presented in this study, a polyhedral mesh (Figure 3b) with a base size of 4.5 mm was employed, as depicted in the figure. An implicit unsteady time step model was utilized, taking a time step of 0.005 s across all simulations, with a total physical simulation time of 2 s. The governing equations, namely the continuity Equation (8) and Reynolds-Averaged Navier–Stokes (RANS) Equation (9) [35], which were utilized in all four simulation scenarios within this study, were discretized using the finite volume method. The turbulence model used for the closure of the Reynolds-Averaged Navier–Stokes equation was the k-ω Menter SST two-layer model [35]. This model was specifically chosen due to its ability to strike a suitable balance between precision, computational efficiency, and robustness.

$$\frac{\partial \rho}{\partial t} + \frac{\partial(\rho v_x)}{\partial x} + \frac{\partial(\rho v_y)}{\partial y} + \frac{\partial(\rho v_z)}{\partial z} = 0 \tag{8}$$

In Equation (8), ρ represents the fluid density, which is a measure of the mass per unit volume. The variable t denotes time, and v_x, v_y, and v_z correspond to the velocity components in the x-, y-, and z-directions, respectively. The term $\frac{\partial \rho}{\partial t}$ represents the rate of change of the density with respect to time. It accounts for how the density of the fluid changes over time within a given volume. Additionally, $\frac{\partial(\rho v_x)}{\partial x}$, $\frac{\partial(\rho v_y)}{\partial y}$, and $\frac{\partial(\rho v_z)}{\partial z}$ represent the rates of change of the mass flow rate density (ρv) with respect to the spatial coordinates x, y, and z, respectively.

$$\rho \frac{\partial U_i}{\partial t} + \rho U_j \frac{\partial U_i}{\partial x_j} = -\frac{\partial P}{\partial x_i} + \frac{\partial}{\partial x_j}\left(2\mu S_{ji} - \rho \overline{u_j' u_i'}\right) \tag{9}$$

The vectors u_i and x_i are the velocity and position, ρ is the density, and s_{ij} is the strain-rate tensor, which is expressed as follows:

$$s_{ij} = \frac{1}{2}\left(\frac{\partial u_i}{\partial x_j} + \frac{\partial u_j}{\partial x_i}\right) \tag{10}$$

Note that $s_{ji} = s_{ij}$.

Equation (9) is referred to as the RANS equation [35]. The quantity $-\rho \overline{u_i' u_j'}$ is known as the Reynolds stress tensor, and we denote it by $\rho \tau_{ij}$, where τ_{ij} is the specific Reynolds stress tensor given by:

$$\tau_{ij} = -\overline{u_i' u_j'} \tag{11}$$

In this study, we assumed that we could simulate the flow of liquid water droplets and the gas phase (primarily air) in a transparent square tube using the Eulerian–Lagrangian (E-L) framework. This framework involved solving the continuity and Navier–Stokes equations (Equations (8) and (9)) for the continuous gas phase and Newton's second law of motion for the individual liquid droplets. The advantages of this approach compared to Eulerian–Eulerian modeling techniques are substantial, as it provides a more detailed understanding of the behavior of discrete particles rather than focusing solely on continuous dynamics. Lagrangian tracking simplifies and reduces the cost of modeling a distribution of particle sizes or other properties of the dispersed phase, which would require separate treatment in the Eulerian technique. Despite its advantages, Eulerian–Lagrangian modeling has limitations. It can be computationally expensive because of the necessity to track a large number of individual particles or parcels, and its computational demands increase with the number of particles being tracked.

We represented the entire population of dispersed phases, specifically liquid droplets, with a reduced number of computational parcels. Each parcel consisted of particles assumed to be spherical, sharing identical properties such as diameter, velocity, density, and temperature. This approach facilitated the modeling of turbulent dispersion. Each parcel was treated as a source term integrated into the governing equations of mass, momentum, and energy at its specific location. Furthermore, we conducted a computational study to determine the optimal number of droplets within each parcel, which enabled us to assess its impact on droplet distribution.

The movement of water droplets was tracked using the Lagrangian multiphase model (LMP). Additionally, we assumed a spherical shape for the droplets, a valid assumption for droplets with a diameter less than 2 mm, as previously mentioned [36]. The NTC (no time counter) collision model was used to simulate the interaction between droplets that occurred during collisions and coalescence, in which colliding droplets stuck together to generate bigger diameter droplets. STAR-CCM+ used the NTC [37] and O'Rourke [38] collision models to identify and forecast the results of interactions between droplets.

In the uncoupled CFD solvers, each velocity component and the pressure field are computed independently based on the flow equations, without considering their mutual interactions. Subsequently, the calculated fields are adjusted to satisfy the continuity equation, and the updated fields are predicted using the SIMPLE algorithm [39]. This approach, known as the segregated approach, was consistently employed in all four simulation cases presented in this study. Boundary conditions provide information on how the flow within the region interacts with its surroundings to STAR-CCM+ solvers. For this study, two boundary conditions were covered: the wall boundary condition and the bottom pressure outlet.

Pre-processing, simulation, and post-processing were performed using Simcenter STAR-CCM+ (version 2020.1, Siemens Product Lifecycle Management Software Inc., Plano, TX, USA). The numerical simulations were carried out on the computer of the Max Planck Research Institute in Magdeburg using an 11th Gen Intel Core I i7-11700 @ 2.50 GHz x64-based processors equipped with 64 GB of RAM.

3. Results and Discussion

Figure 2 shows the coalescence along with the stretching and breakup of droplets. For two nozzle plates (N1 to N2) with different vertical distances between the camera's focus frame and nozzle plate, the frequency distribution of the measured droplet size was plotted, and their standard deviation, kurtosis, and skewness were calculated, as shown in Table 2. A standard deviation is a measure of how dispersed the data (droplet sizes) are in relation to the mean value. When examining nozzle plates N1 and N2, it became evident, as shown in Table 2, that the standard deviation increased as the vertical distance (H) between the camera's focus frame and the nozzle plate expanded. Furthermore, the arithmetic mean d_{10} (µm) exhibited a corresponding increase with the vertical height (H) for both nozzle plates (N1 and N2), ranging from H0 to H2. The increase (10–15%)

in the arithmetic mean and standard deviation was a consequence of the collisions and coalescence among the droplets.

Skewness is an important statistical technique that helps determine the asymmetrical behavior of the frequency distribution, or more precisely, the lack of symmetry of tails on both the left and right sides of the frequency curve. A positive value of skewness means the right tail of the frequency curve is longer than the left tail, whereas a negative value indicates the opposite. In the context of the N1H0 and N2H0 experiments, this suggests that the initial droplet size distribution (0 mm) may conform to a log-normal distribution. The results, depicted in Figures 4 and 5, demonstrate a fairly acceptable fit with a log-normal distribution.

Kurtosis is a measure of whether the data are heavy-tailed or light-tailed relative to a normal distribution. That is, data sets with high kurtosis tend to have heavy tails, whereas those with low kurtosis tend to have light tails. In the case of the N1H0 and N2H0 experiments, the value of kurtosis is high, which means the droplet size distribution curve must have heavy tails.

Table 2. Experimentally measured SMD, standard deviation, kurtosis, and skewness of droplet size distribution.

Exp. Run Case	Arithmetic Mean, µm	Standard Deviation, µm	Kurtosis	Skewness
N1H0	342	90	1.37	0.91
N1H1	394	121	−0.56	0.24
N1H2	462	169	−0.79	0.18
N2H0	369	95	7.0	2.21
N2H1	470	164	1.3	1.0
N2H2	445	180	0.27	0.77

3.1. Droplet Size Distribution

A log-normal distribution is a continuous probability distribution of a random variable whose logarithm is normally distributed. If the water droplet diameter (d) is log-normally distributed, then ln(d) has a normal distribution with a log mean μ and standard deviation σ, as shown in Figures 4 and 5.

The above-mentioned log-normal distribution uses the following mean and standard deviation (SD) formulas [40] for the droplet diameter (d):

$$\text{Mean } = e^{\left(\mu + \frac{\sigma^2}{2}\right)} \tag{12}$$

$$SD = \sqrt{e^{2(\mu+\sigma^2)} - e^{(2\mu+\sigma^2)}} \tag{13}$$

As illustrated in Figure 4, the measured droplet diameter right after injection moderately fits the log-normal distribution, with an R^2 value ≥ 0.9.

A z-score, often referred to as a standard score, provides valuable insight into the deviation of a data point from the population mean. To be more precise, it quantifies the number of standard deviations by which a droplet diameter falls below or exceeds the population mean.

$$\ln(d) = \sigma z + \mu \tag{14}$$

$$z = \frac{d - \text{ Mean}}{SD} \tag{15}$$

For the normal distribution of droplets, the following equation was used:

$$d = \sigma z + \mu \tag{16}$$

where d represents the droplet diameter (µm), μ represents the mean (µm), and σ represents the standard deviation (µm) for normally distributed data. A normal distribution is defined

as a probability distribution that is symmetric about the mean, showing that data near the mean are more frequent in occurrence compared to data far from the mean, which is also known as a Gaussian distribution.

From Figures 4a and 5b, it is clear that the quantile–quantile plots exhibit fairly good fitting with R^2 values larger than 0.9. Therefore, we can conclude that the model fits well with the data, and we used this log-normal distribution as an input parameter (water droplet distribution) in the respective CFD simulations.

3.2. Computational Fluid Dynamics Simulations

The digital twin of the experimental setup for the N1H1 and N1H2 cases was built (Figure 3). It used the log-normal distribution depicted in Figure 4b as the input diameter distribution for the CFD simulations. These simulations involved the injection of droplets from 17 or 30 points on the nozzle plate, employing the numerical implementation of the Eulerian–Lagrangian (E-L) approach for multiphase flows in both cases.

3.2.1. Mesh Independence Study

The results of a CFD model can be altered depending on the mesh imposed onto the geometry. To obtain more accurate results, choosing an appropriate mesh configuration is essential. It has been found that smaller meshes tend to produce better solutions with increased precision [41]. However, this requires utilizing a finer resolution for the simulation, which increases computing power, as more equations must be solved to complete the task. Thus, selecting the appropriate mesh involves balancing accuracy and computational ability. Before running the CFD simulations, a mesh independence test was conducted to determine the most suitable grid size for this numerical study. Three meshes (M1: 3.5 mm; M2: 4.5mm; and M3: 5.5 mm base size) were utilized and examined to understand how they impacted water droplet diameter distribution, as shown in Figure 6. The results depicted in Figure 6 show that the mesh's base size did not have a significant effect on the water droplet diameter distribution plots, which remained unchanged and steady for the respective case. Taking into account computational efficiency, it was decided that a 4.5 mm base-size polyhedral mesh would be used (with 266,016 mesh cells).

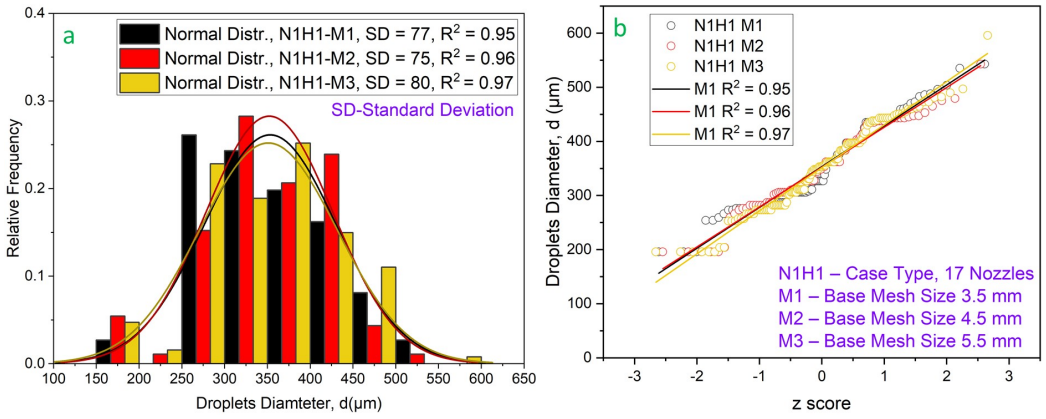

Figure 6. (**a**) Mesh independence study. (**b**) Normal distribution fitting (Q−Q plot) with linear fit of R^2 for N1H1.

3.2.2. Unsteady Inner Iteration Study

The maximum inner iteration stopping criterion is determined by the number of inner iterations performed by the solver during a CFD simulation. This stopping criterion can be used to constrain the number of inner iterations that must be performed at each physical time step. To determine the optimum number of unsteady inner iterations for the numerical investigation, unsteady inner iteration independence testing was carried out. Three distinct inner iteration numbers, in increments of 5, were examined to determine their influence on the distribution of water droplet diameters. Unsteady inner iterations did not significantly

affect the final results, as demonstrated in Figure 7. For all CFD simulations, 15 unsteady inner iterations were selected as the standard because they yielded identical results to 20 iterations. This choice was made to optimize computational efficiency, as higher iteration numbers require increased computational time without providing additional accuracy or insights.

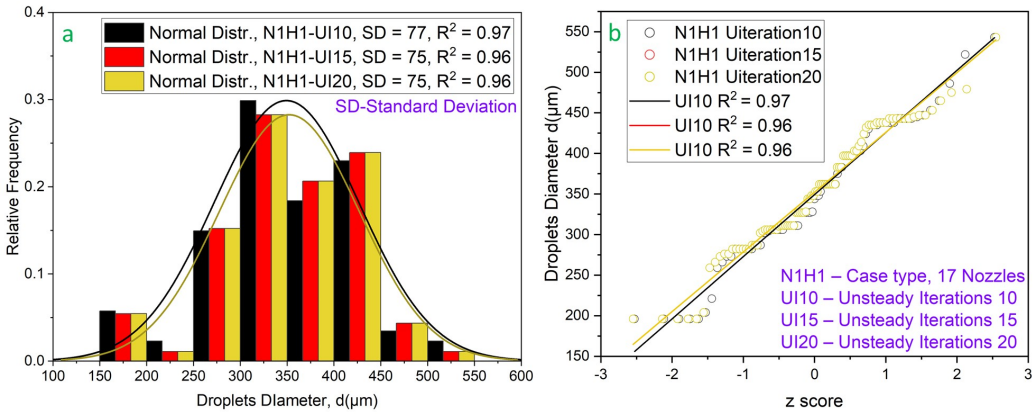

Figure 7. (**a**) Unsteady inner iteration independence study. (**b**) Normal distribution fitting (Q-Q plot) with linear fit of R^2 for N1H1.

3.2.3. Parcel Study

In unsteady simulations, this parameter (number of parcels) determines the number of parcel streams for each time step. The resolution of the particle size distribution increases with the number of parcel streams. For this purpose, 5–20 parcel streams are typically defined [36]. Therefore, a study on parcel independence is essential to understand how it affects the distribution of droplet diameters. To determine the optimum number of parcel streams for this numerical analysis, parcel stream independence testing was performed. To determine the impact on the distribution of water droplet diameter, three different numbers of parcel streams (9, 10, and 11) were investigated. Figure 8 demonstrates that the number of parcel streams had a reasonable impact on the distributions of droplet diameters, and increasing the number of parcels significantly increased the computing time. Therefore, ten parcel streams were selected for further CFD simulation studies to balance computational time and accuracy.

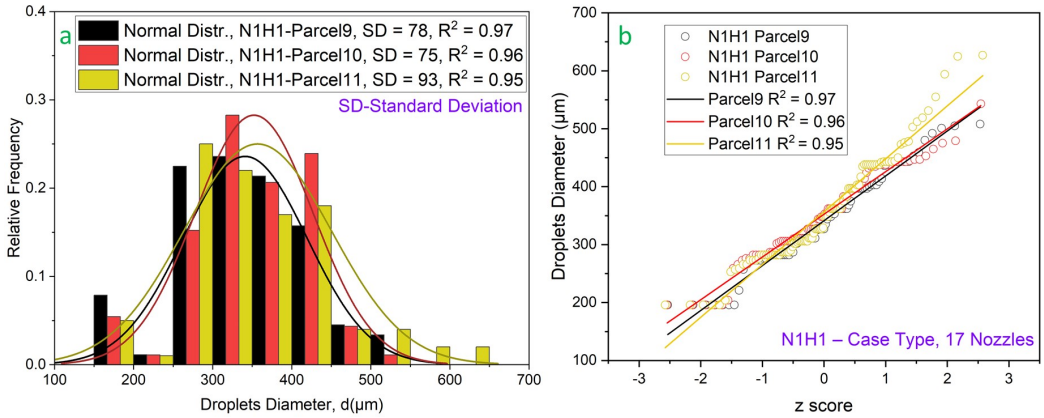

Figure 8. (**a**) Computational parcel study. (**b**) Normal distribution fitting (Q−Q plot) with linear fit of R^2 for N1H1.

3.2.4. CFD Model Validation with Experiments

CFD simulations were performed to investigate four distinct scenarios: N1H1, N1H2, N2H1, and N2H2. In all four scenarios, the simulations involved the injection of water droplets through nozzles situated at the shower head. These water droplets were treated

as Lagrangian particles and introduced into the computational domain. The initiation of water droplet ejection from nozzles was facilitated by an initial injection velocity ($\dot{q}_l$, flowrate/a, area) specified within the CFD simulation parameters. The downward motion of these droplets was primarily governed by the gravitational force acting in the negative y-direction.

As the water droplets fell, they dynamically interacted with the initially stagnant air within the square tube. This interaction caused the stationary air to move, leading to the formation of air-velocity profiles in the CFD simulation domain.

Figure 9 presents the air-velocity profiles generated in two CFD cases: N1H1 and N1H2. These profiles demonstrate the evolving airflow patterns resulting from the falling of the water droplets. As the water droplets descended from the shower head, their velocity increased due to gravitational effects, droplet collisions, and coalescence. Consequently, the air movement intensified around the droplets, as depicted in Figure 9. Notably, the air-velocity profile became more pronounced as the distance from the injection point (shower head) increased.

The simulation results were compared to the experimental droplet size distribution and Sauter mean diameter (d_{32}) recorded at distances of 200 mm and 400 mm from the nozzle plate inlet for both the N1H1 and N1H2 cases, as outlined in Table 3. The results from both the experimental observations and simulations indicated that at the nozzle inlet, the droplet size distribution followed a log-normal pattern. However, at greater distances from the shower head, specifically at 200/400 mm, the droplet size distribution exhibited a reasonably good fit to a normal distribution. This trend is visualized in Figures 10–13.

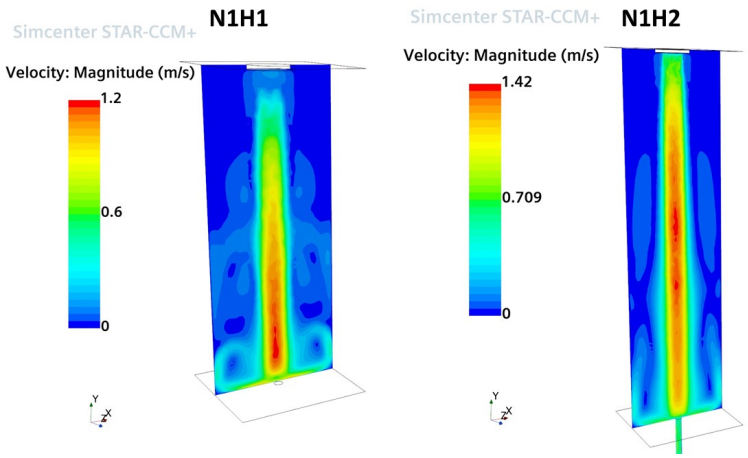

Figure 9. Air-velocity contour plot of square column for N1H1 and N1H2.

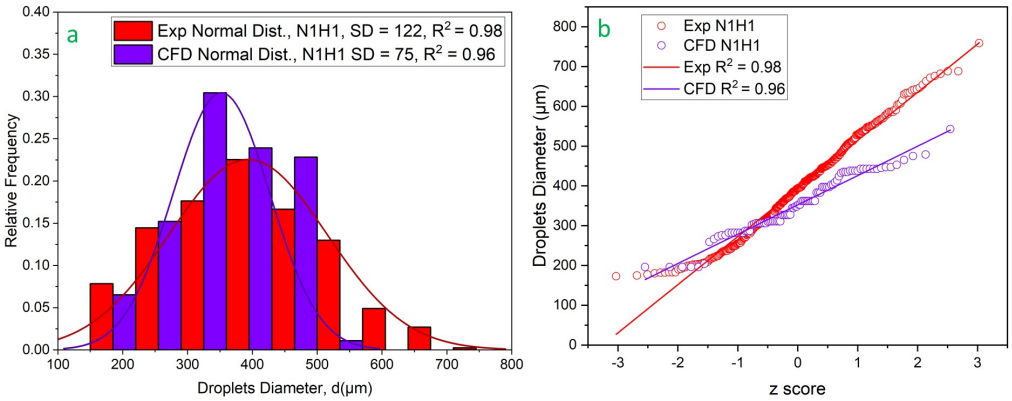

Figure 10. (**a**) Experimental and CFD droplet size frequency distributions with fitted curves. (**b**) Normal distribution fitting (Q−Q plot) with linear fit of R^2 for N1H1.

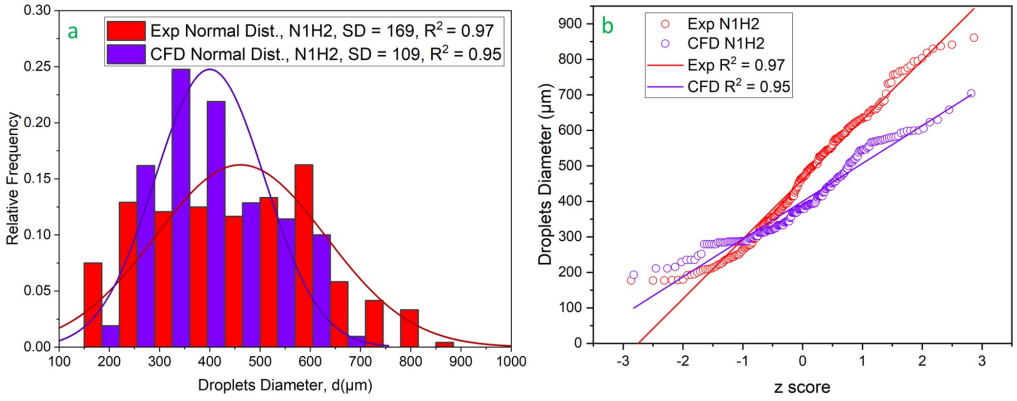

Figure 11. (**a**) Experimental and CFD droplet size frequency distributions with fitted curves. (**b**) Normal distribution fitting (Q−Q plot) with linear fit of R^2 for N1H2.

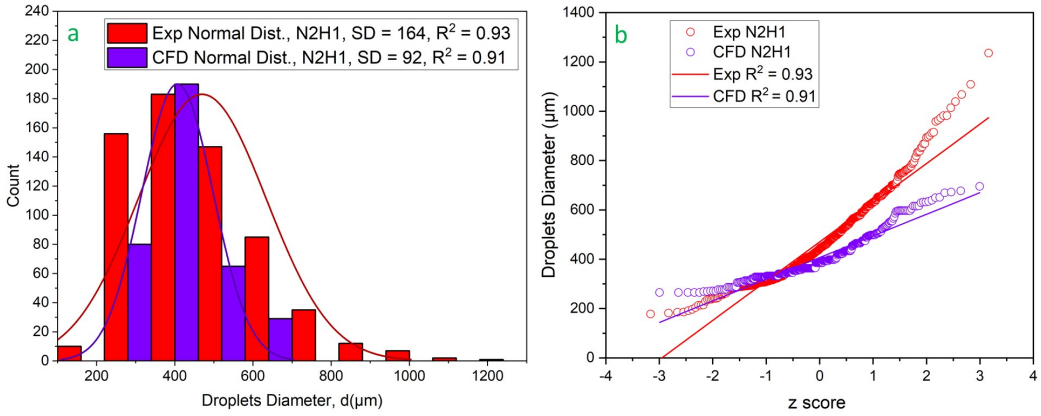

Figure 12. (**a**) Experimental and CFD droplet size frequency distributions with fitted curves. (**b**) Normal distribution fitting (Q−Q plot) with linear fit of R^2 for N2H1.

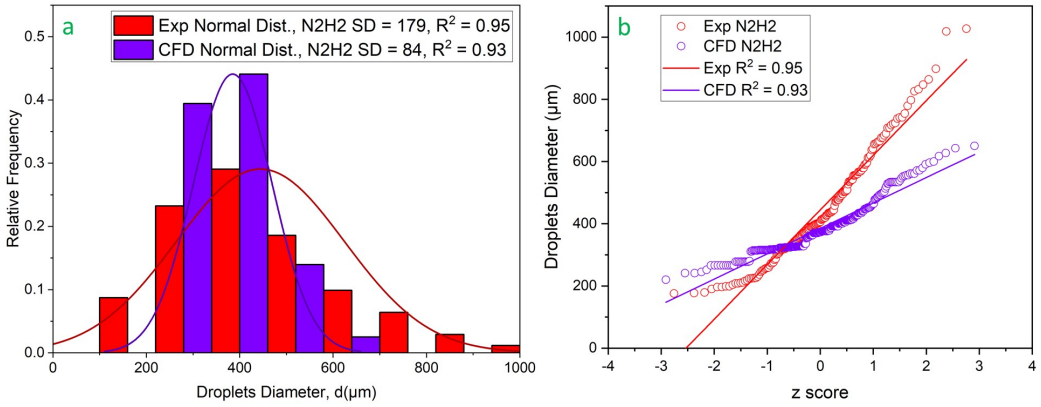

Figure 13. (**a**) Experimental and CFD droplet size frequency distributions with fitted curves. (**b**) Normal distribution fitting (Q−Q plot) with linear fit of R^2 for N2H2.

In the N1H1 CFD case, the total length between the shower head and the bottom of the square tube was 370 mm, whereas in the N1H2 case, it was 570 mm (Figure 3). Figure 9 illustrates that in the N1H1 CFD case, a moderate vortex of the air-velocity profile was formed. Conversely, in the N1H2 case, the intensity of the vortex, or the development of the air-velocity profile, was reduced. This disparity can be attributed to the greater length of the CFD domain in N1H2 compared to N1H1.

Table 3. Comparison of diameter means (d_{10}, d_{20}, d_{30}, and d_{32}) between experimental data and CFD simulations for the respective run cases.

Run Case	Arithmetic Mean d_{10} (µm)			Surface Area Mean d_{20} (µm)			Volume Mean d_{30} (µm)			Sauter Mean Diam. d_{32} (µm)		
	Exp.	CFD	Diff. %	Exp.	CFD	Diff. %	Exp.	CFD	Diff. %	Exp.	CFD	Diff. %
N1H1	393	352	10	411	360	12	428	367	14	464	382	17
N1H2	461	400	13	491	414	15	517	429	17	575	459	20
N2Hl	470	406	13	497	416	16	526	427	18	590	450	23
N2H2	444	385	13	479	394	17	513	404	21	588	424	27

Table 3 presents a comparative analysis of the average mean diameters, namely d_{10}, d_{20}, d_{30}, and d_{32}, for liquid droplets at two distinct heights—200 mm and 400 mm—across both nozzle plates. The difference between the experimental and CFD-derived arithmetic mean ranged from 10 to 13%, indicating a moderate level of confidence in the CFD model's ability to accurately predict the arithmetic mean diameter of water droplets at different elevations.

Furthermore, for the surface area mean, the difference between the experimental data and CFD simulations ranged from 12 to 17%. However, for the volume mean and Sauter mean diameter, the disparities were higher, falling within the range of 14–27%. This observation highlights larger variations between the experimental and simulated results, particularly for the volume mean and Sauter mean diameter metrics.

The arithmetic mean exhibited a better fit than the Sauter mean diameter when comparing the experimental and CFD simulation results. This is because the arithmetic mean was less affected by extreme values. The arithmetic mean simply calculated the average of all droplet sizes, whereas the Sauter mean was more influenced by the ratio of the volume-to-surface area, making it more sensitive to variations in the distribution's range.

From Table 3, it is evident that the experimental mean was consistently larger than the CFD mean. This suggests that the CFD simulations tended to underestimate the droplet diameter. The observed disparity between the CFD simulation and experimental results could be attributed to the use of a fitted log-normal distribution in the simulations. This distribution, while providing a continuous representation, introduced errors and may not have accurately captured the real droplet size distribution, which potentially included larger droplets. In a continuous size distribution, there tends to be less coalescence due to the smoother variation in droplet velocities. Conversely, experiments with a discontinuous distribution may exhibit more significant differences in droplet velocities, potentially leading to increased coalescence. One potential enhancement for the model could involve using the actual population of droplets instead of a fitted distribution. However, implementing this approach becomes challenging in practical scenarios with numerous nozzle holes. Additionally, the assumption in the CFD simulation that droplets are perfectly spherical reduces the likelihood of collisions and coalescence, given the minimized collision surface area. In addition to the assumptions related to droplet size distribution and spherical shapes, another significant assumption in the CFD simulation is the uniform injection velocity for all droplets. While a size distribution was considered, an injection velocity distribution was not incorporated. This assumption implies that all droplets share the same initial velocity upon injection, contributing to an underestimation of collisions in the simulation. In reality, droplets often exhibit a range of velocities, and neglecting this variation in the CFD model leads to an oversimplified representation. The consequence is a diminished prediction of collisions, as the uniform velocity assumption diminishes the potential for differences in droplet velocities that would contribute to collision events. Addressing this limitation by incorporating a more realistic distribution of injection velocities could enhance the accuracy of the CFD model in predicting collision and coalescence phenomena.

Figures 10–13 depict the experimental and CFD droplet size frequency distributions, accompanied by fitted normal distribution curves and linear fits of R-squared values for

runs N1H1 to N2H2, respectively. There is a significant difference in the standard deviation of droplet sizes between the experimental results and the CFD simulations. This difference can be attributed to the inherent assumptions and limitations of the NTC model used in the CFD simulations for modeling droplet dynamics. While the NTC model effectively captures the average droplet size, it may not fully represent certain physical processes involved in droplet formation and behavior. This partial representation could lead to a realistic estimation of the mean diameter, yet produce a variation in the droplet size distribution that differs from what is observed experimentally. This discrepancy underscores the complexity of accurately modeling droplet interactions and dynamics and highlights the need for careful consideration of model selection and parameterization in CFD simulations.

It is interesting to note that when droplets are at a height (H0) of 0 mm, their diameter distribution can be adequately characterized by a log-normal curve. Nevertheless, the log-normal distribution eventually changes into a normal distribution as these droplets start to fall. This shift suggests that the processes of collision and coalescence are predominantly influenced by a normal probability function. The transition from an initial log-normal distribution of water droplets to a normal distribution as these droplets descend within a square tube over an increased height is the result of a complex interplay of various contributing factors. First and foremost, the process of coalescence comes into play as the droplets interact and collide within the confined space of the tube. This collision-induced merging and growth of droplets lead to a gradual shift in the distribution pattern, eventually aligning it with a normal distribution.

One key factor that plays a crucial role in this transformation is the Weber number (We), a dimensionless number used in fluid dynamics to predict when the inertial forces of a fluid become dominant over its surface tension [42]. A Weber number significantly less than 1 (We « 1) signifies that surface tension forces are dominant, ensuring that the droplets remain intact throughout the CFD domain. When examining droplets through CFD simulations, it has been consistently observed that the Weber number remains below 0.14. This observation suggests that droplet breakup is not occurring due to the dominance of inertial forces. When the Weber number is less than 0.14, the inertial forces are typically not strong enough to overcome the cohesive forces holding the droplet together, thus preventing breakup. In summary, the complex interaction between gravity, air resistance, droplet collisions, and coalescence leads to the change of droplet sizes from an initial log-normal distribution to a normal distribution inside a square tube.

4. Conclusions

Our primary objective was to measure the size distribution of droplets along a droplet absorber and validate CFD simulations based on their prediction capability. The obtained results indicate that the droplet size distribution was predicted through CFD simulations, with errors in the range of 11–27%. Our results show that at the nozzle inlet, a log-normal distribution of droplet sizes was well matched, as evidenced by an R^2 value greater than 0.90. Furthermore, at distances of 200 mm and 400 mm from the nozzle inlet, a normal distribution of droplet sizes showed a reasonably good fit. The Lagrangian–Eulerian multi-phase CFD simulations provided satisfactory approximations of both the arithmetic mean droplet diameter and its corresponding distributions for the investigated cases. The CFD model demonstrates significant potential for broader applications, offering the capability to predict droplet sizes and distributions across a variety of geometric setups and nozzle configurations, with a certain margin of error. Its adaptability is particularly noteworthy within the Rayleigh regime of flow rates, showcasing its versatility and practical utility.

Supplementary Materials: The following supporting information can be downloaded at: www.mdpi.com/xxx/s1, Figure S1: (a) Camera calibration plate. (b) Front view and (c) Angled view of Calibration setup.; Figure S2: Measure the real distances between shapes; Figure S3: ozzle diameter measurements.

Author Contributions: Conceptualization, P.S. and K.V.; methodology, K.V., G.J. and P.S.; software, K.V. and G.J.; validation, K.V. and P.S.; investigation, K.V.; writing—original draft preparation, K.V.; writing—review and editing, K.V., G.J., H.L., A.S.-M., M.F.G. and P.S.; supervision, P.S. and G.J.; project administration, H.L. and P.S.; funding acquisition, A.S.-M. and P.S. All authors have read and agreed to the published version of the manuscript.

Funding: This research was funded by the BMBF (No. 01LJ2003B).

Institutional Review Board Statement: Not applicable.

Informed Consent Statement: Not applicable.

Data Availability Statement: The data presented in this study are available in the OSF data repository, accessible via this link: https://doi.org/10.17605/OSF.IO/9RM2B.

Acknowledgments: The authors extend sincere gratitude to the dedicated staff of the Max Planck Institute for Dynamics of Complex Technical Systems Magdeburg for their invaluable support throughout the project. Further, we thank our industrial partner, the CIECH group, for their cooperation and the company SChPrEngCo for initiating the CODA project.

Conflicts of Interest: The authors declare no conflicts of interest.

Abbreviations

The following abbreviations are used in this manuscript:

CFD	Computational Fluid Dynamics
VOF	Volume of Fluid
MEA	Monoethanolamine
USAXS	Ultra-Small-Angle X-ray Scattering
PMMA	Poly methyl methacrylate
RGB	Red, Green, and Blue
RANS	Reynolds-Averaged Navier–Stokes
SD	Standard Deviation
Q-Q	Quantile–Quantile
LE	Lagrangian–Eulerian
NTC	No Time Counter

References

1. Thybo, P.; Hovgaard, L.; Andersen, S.K.; Lindeløv, J.S. Droplet size measurements for spray dryer scale-up. *Pharm. Dev. Technol.* **2008**, *13*, 93–104. [CrossRef]
2. Koračin, N.; Zupančič, M.; Vrečer, F.; Hudovornik, G.; Golobič, I. Characterization of the spray droplets and spray pattern by means of innovative optical microscopy measurement method with the high-speed camera. *Int. J. Pharm.* **2022**, *629*, 122412. [CrossRef]
3. Cha, H.; Ma, J.; Kim, Y.S.; Li, L.; Sun, L.; Tong, J.; Miljkovic, N. In situ droplet microgoniometry using optical microscopy. *ACS Nano* **2019**, *13*, 13343–13353. [CrossRef]
4. Pei, Y.; Hinchliffe, B.A.; Minelli, C. Measurement of the size distribution of multimodal colloidal systems by laser diffraction. *ACS Omega* **2021**, *6*, 14049–14058. [CrossRef]
5. Raman, R.K.; Dewang, Y.; Raghuwanshi, J. A review on applications of computational fluid dynamics. *Int. J. LNCT* **2018**, *2*, 137–143.
6. Montazeri, H.; Blocken, B.; Hensen, J. Evaporative cooling by water spray systems: CFD simulation, experimental validation and sensitivity analysis. *Build. Environ.* **2015**, *83*, 129–141. [CrossRef]
7. Nijdam, J.J.; Guo, B.; Fletcher, D.F.; Langrish, T.A. Lagrangian and Eulerian models for simulating turbulent dispersion and coalescence of droplets within a spray. *Appl. Math. Model.* **2006**, *30*, 1196–1211. [CrossRef]
8. Pinto, M.; Kemp, I.; Bermingham, S.; Hartwig, T.; Bisten, A. Development of an axisymmetric population balance model for spray drying and validation against experimental data and CFD simulations. *Chem. Eng. Res. Des.* **2014**, *92*, 619–634. [CrossRef]
9. Chot-Plassot, P.; Vignes, A.; Murillo, C.; Lacome, J.M.; El-Zahlanieh, S.; Bardin-monnier, N.; Dufaud, O. Combining CFD and Experimental Approaches to Optimize a Spray Release in a 20 L Sphere. In Proceedings of the 17th International Symposium on Loss Prevention and Safety Promotion in the Process Industry, Prague, Czech Republic, 5–8 June 2022; AIDIC: Milan, Italy, Volume 90, pp. 397–402.

10. Beji, T.; Zadeh, S.E.; Maragkos, G.; Merci, B. Influence of the particle injection rate, droplet size distribution and volume flux angular distribution on the results and computational time of water spray CFD simulations. *Fire Saf. J.* **2017**, *91*, 586–595. [CrossRef]
11. Frühhaber, J.; Lieber, C.; Mattes, D.; Lauer, T.; Koch, R.; Bauer, H.J. Modeling the Formation of Urea-Water Sprays from an Air-Assisted Nozzle. *Appl. Sci.* **2020**, *10*, 5723. [CrossRef]
12. Mahmud, H.I.; Thorpe, G.; Moinuddin, K.A. An Approach to Determine the Median Diameter of Droplets in a Water-Mist Spray. *Appl. Sci.* **2022**, *12*, 1073. [CrossRef]
13. Rossano, V.; De Stefano, G. Hybrid VOF–Lagrangian CFD Modeling of Droplet Aerobreakup. *Appl. Sci.* **2022**, *12*, 8302. [CrossRef]
14. Dimiccoli, A.; Di Serio, M.; Santacesaria, E. Mass transfer and kinetics in spray-tower-loop absorbers and reactors. *Ind. Eng. Chem. Res.* **2000**, *39*, 4082–4093. [CrossRef]
15. Saber, F.; Abdelsamie, A.; Sedrak, M. Numerical investigation of particle spray size distribution in turbulent jet flow. *Eng. Res. J.* **2022**, *174*, 262–284. [CrossRef]
16. Bade, K.; Kalata, W.; Schick, R. Experimental and computational study of a spray at multiple injection angles. In Proceedings of the ILASS Americas, 22nd Annual Conference on Liquid Atomization and Spray Systems, Cincinnati, OH, USA, 17–19 May 2010.
17. Tamhankar, Y.; King, B.; Whiteley, J.; Cai, T.; McCarley, K.; Resetarits, M.; Aichele, C. Spray absorption of CO_2 into monoethanolamine: Mass transfer coefficients, dropsize, and planar surface area. *Chem. Eng. Res. Design* **2015**, *104*, 376–389. [CrossRef]
18. Tamhankar, Y.; King, B.; Whiteley, J.; McCarley, K.; Cai, T.; Resetarits, M.; Aichele, C. Interfacial area measurements and surface area quantification for spray absorption. *Sep. Purif. Technol.* **2015**, *156*, 311–320. [CrossRef]
19. Cho, M.; Lee, S.; Choi, M.; Lee, J.W. Novel spray tower for CO_2 capture using uniform spray of monosized absorbent droplets. *Ind. Eng. Chem. Res.* **2018**, *57*, 3065–3075. [CrossRef]
20. Foissac, A.; Malet, J.; Vetrano, R.; Buchlin, J.; Mimouni, S.; Feuillebois, F.; Simonin, O. Experimental measurements of droplet size and velocity distributions at the outlet of a pressurized water reactor containment swirling spray nozzle. *At. Sprays* **2011**, *21*, 893–905. [CrossRef]
21. Cents, A.; Brilman, D.W.F.; Versteeg, G.; Wijnstra, P.; Regtien, P.P. Measuring bubble, drop and particle sizes in multiphase systems with ultrasound. *AIChE J.* **2004**, *50*, 2750–2762. [CrossRef]
22. Kastengren, A.; Ilavsky, J.; Viera, J.P.; Payri, R.; Duke, D.J.; Swantek, A.; Tilocco, F.Z.; Sovis, N.; Powell, C.F. Measurements of droplet size in shear-driven atomization using ultra-small angle X-ray scattering. *Int. J. Multiph. Flow* **2017**, *92*, 131–139. [CrossRef]
23. Frommhold, P.E.; Lippert, A.; Holsteyns, F.L.; Mettin, R. High-speed monodisperse droplet generation by ultrasonically controlled micro-jet breakup. *Exp. Fluids* **2014**, *55*, 1716. [CrossRef]
24. Musiu, E.M.; Qi, L.; Wu, Y. Evaluation of droplets size distribution and velocity pattern using Computational Fluid Dynamics modelling. *Comput. Electron. Agric.* **2019**, *164*, 104886. [CrossRef]
25. Cao, Y.; Xi, T.; Xu, L.; Qiu, W.; Guo, H.; Lv, X.; Li, C. Computational fluid dynamics simulation experimental verification and analysis of droplets deposition behaviour on vibrating pear leaves. *Plant Methods* **2022**, *18*, 80. [CrossRef]
26. Wirz, D.; Friebel, A.; Rave, K.; Hermes, M.; Skoda, R.; von Harbou, E.; Bart, H.J. Experimental Investigation and Modelling of the Droplet Size in a DN300 Stirred Vessel at High Disperse Phase Content Using a Telecentric Shadowgraphic Probe. *Appl. Sci.* **2022**, *12*, 4069. [CrossRef]
27. Melnikova, V.G.; Epikhin, A.S.; Kraposhin, M.V. The Eulerian–Lagrangian Approach for the Numerical Investigation of an Acoustic Field Generated by a High-Speed Gas-Droplet Flow. *Fluids* **2021**, *6*, 274. [CrossRef]
28. Schindelin, J.; Arganda-Carreras, I.; Frise, E.; Kaynig, V.; Longair, M.; Pietzsch, T.; Preibisch, S.; Rueden, C.; Saalfeld, S.; Schmid, B.; et al. Fiji: An open-source platform for biological-image analysis. *Nat. Methods* **2012**, *9*, 676–682. [CrossRef]
29. Liu, H. *Science and Engineering of Droplets: Fundamentals and Applications*; William Andrew: Norwich, NY, USA, 1999.
30. Mitchell, B.R.; Klewicki, J.C.; Korkolis, Y.P.; Kinsey, B.L. Normal impact force of Rayleigh jets. *Phys. Rev. Fluids* **2019**, *4*, 113603. [CrossRef]
31. Rueden, C.T.; Schindelin, J.; Hiner, M.C.; DeZonia, B.E.; Walter, A.E.; Arena, E.T.; Eliceiri, K.W. ImageJ2: ImageJ for the next generation of scientific image data. *BMC Bioinform.* **2017**, *18*, 529. [CrossRef]
32. Yen, J.C.; Chang, F.J.; Chang, S. A new criterion for automatic multilevel thresholding. *IEEE Trans. Image Process.* **1995**, *4*, 370–378.
33. Siritantikorn, S.; Jintaworn, S.; Noisakran, S.; Suputtamongkol, Y.; Paris, D.H.; Blacksell, S.D. Application of ImageJ program to the enumeration of Orientia tsutsugamushi organisms cultured in vitro. *Trans. R. Soc. Trop. Med. Hyg.* **2012**, *106*, 632–635. [CrossRef]
34. Sauter, J. *Die Grössenbestimmung der im Gemischnebel von Verbrennungskraftmaschinen Vorhandenen Brennstoffteilchen (Mitteilg aus d. Laboratorium f. techn. Physik d. Techn. Hochschule München)*; Forschungsarbeiten auf dem Gebiete des Ingenieurwesens; VDI-Verlag: Berlin, Germany, 1926.
35. Wilcox, D. *Turbulence Modeling for CFD*; DCW Industries: La Canada, CA, USA, 2006.
36. *STAR-CCM+*, version 2020.1; Software Manual. Siemens Product Lifecycle Management Software, Inc.: Plano, TX, USA, 2020.
37. Bhatia, B.; Johny, T.; De, A. Understanding the liquid jet break-up in various regimes at elevated pressure using a compressible VOF-LPT coupled framework. *Int. J. Multiph. Flow* **2023**, *159*, 104303. [CrossRef]
38. O'Rourke, P.J. Collective Drop Effects on Vaporizing Liquid Sprays. Ph.D. Thesis, Princeton University, Princeton, NJ, USA, 1981.

39. Ferziger, J.H.; Perić, M. *Computational Methods for Fluid Dynamics*; Springer: Berlin/Heidelberg, Germany, 2002.
40. Lahcene, B. Extended lognormal distribution: Properties and applications. *World Sci. News* **2020**, *145*, 16–30.
41. Sande, P.; Ray, S. Mesh size effect on CFD simulation of gas-fluidized Geldart A particles. *Powder Technol.* **2014**, *264*, 43–53. [CrossRef]
42. Li, D. (Ed.) Weber Number. In *Encyclopedia of Microfluidics and Nanofluidics*; Springer: Boston, MA, USA, 2008; p. 2185.